Research Article | Vol. 34, No. 16 / 10 Aug 2026 / Optics Express 29435
Optics EXPRESS

Fabrication-robust, high-FSR, low-crosstalk mode-selective microring resonators

TOBIAS ZYPMAN,[1,*] BRETT GEORGE,[1] ROBERT PARSONS,[2] XIANG MENG,[1] AND KEREN BERGMAN[1]

[1] Department of Electrical Engineering, Columbia University, New York, New York 10027, USA
[2] Xscape Photonics Inc., Fort Lee, NJ 07024, USA
[*] tz2589@columbia.edu

Abstract: Mode-division multiplexing (MDM) has emerged as a promising approach for increasing optical interconnect bandwidth density by enabling multiple spatial channels within a single waveguide. In this work, we demonstrate fabrication-robust, high-free spectral range (FSR), and low-crosstalk mode-selective silicon microring resonators (MRRs) for the TE_0, TE_1, TE_2, and TE_3 spatial modes. By engineering the phase matching conditions between a single-mode ring resonator and multimode bus waveguides, we realize mode- and wavelength-selective filtering while maintaining a compact 5 µm ring radius. The fabricated TE_1, TE_2, and TE_3 devices exhibit nominal crosstalk suppression values of 30.3 dB, 39.1 dB, and 28.8 dB, respectively. All fabricated devices demonstrate extinction ratios greater than 23.1 dB, full width at half maximum (FWHM) greater than 71.7 GHz, and FSRs up to 14.9 nm. Eye diagram and bit error rate (BER) measurements further demonstrate 25 Gb/s transmission using NRZ PRBS31 signals with BERs below 10^{-12} for received optical powers of −7.5 dBm and above for all fabricated MRRs, with all eye diagrams remaining clearly open. Fabrication variation analysis further demonstrates robust operation under representative dimensional variations in waveguide geometry, with all fabricated device variations maintaining crosstalk suppression between 23 dB and 40 dB between the desired mode and all lower-order modes.

1. Introduction

The rapid expansion of AI workloads and data-intensive computing has led to unprecedented growth in the demand for high-speed optical interconnects in data centers and high performance computing (HPC) systems [1–4]. Mode-division multiplexing (MDM) has emerged as a particularly promising approach for increasing optical interconnect bandwidth density, leveraging multiple orthogonal spatial modes within a waveguide to transmit parallel data channels [5,6]. By enabling several independent channels within a single waveguide, MDM can substantially increase both data throughput and spectral efficiency [7–11]. MDM has been widely explored for use in data transmission [12,13], photonic signal processing [14], spatial switching [15–17], and quantum photonics [18–20]. As a result, significant efforts have been made to design integrated multimode photonic devices for mode multiplexing, filtering, routing, and switching [21]. Among the devices enabling these functionalities, microring resonators (MRRs) are particularly attractive due to their compact footprint, wavelength selectivity, and compatibility with large-scale photonic integration [22]. Mode-selective MRRs further extend these capabilities by enabling simultaneous mode and wavelength selectivity [23–25]. However, simultaneously achieving high free spectral range (FSR), low crosstalk, and selective coupling to higher-order spatial modes in compact MRRs remains challenging due to phase matching requirements and fabrication-induced modal coupling. Previous demonstrations of mode-selective MRRs have therefore often been constrained by low FSR, limited crosstalk suppression, or operation restricted to lower-order spatial modes. A comparison of representative mode-selective MRR demonstrations is summarized in Table 1.

#606904 https://doi.org/10.1364/OE.606904
Journal © 2026 Received 28 May 2026; revised 30 Jun 2026; accepted 8 Jul 2026; published 30 Jul 2026

Optics EXPRESS

Table 1. Comparison of mode-selective microring resonator (MRR) demonstrations. *XT*: crosstalk suppression; *FSR*: free spectral range; *ER*: extinction ratio; *Fab. Var.*: fabrication variations; *R*: radius; L_c: coupling length. "–" indicates the metric was not explicitly reported.

Reference	Platform	Highest Mode	Ring Size	XT (dB)	FSR (nm)	ER (dB)	Data Rate	Fab. Var.
Luo *et al.* [7]	Si	TE_2	$R = 10\,\mu m,\ L_c = 5\,\mu m$	12–22	–	–	10 Gb/s[a]	No
Jia *et al.* [13]	Si	TE_3	$R = 20\,\mu m$	19.7–25.1	5	–	50 Gb/s	No
Stern *et al.* [15]	Si	TE_1	$R = 16\,\mu m$	16.8–24[b]	5	–	10 Gb/s[a]	No
Han *et al.* [23]	Si	TE_1	$R = 10\,\mu m$	16–22	–	>20	10 Gb/s	No
Jia *et al.* [24]	Si	TE_3	$R = 10\,\mu m,\ L_c = 2\,\mu m$	10.8–13.7	9.1	19.6–20.6	50 Gb/s	No
Yang *et al.* [25]	SiN	TE_2	$R = 30\,\mu m$	10–18	–	–	30 Gb/s	No
This work	**Si**	$\mathbf{TE_3}$	$\mathbf{R = 5\,\mu m,\ L_c = 2.46\,\mu m}$	**28.8–39.1**	**14.9**	**>23**	**25 Gb/s**[a]	**Yes**

[a]BER $<10^{-12}$ experimentally demonstrated.
[b]Reported for the complete switch architecture, not an individual mode-selective MRR.

In this work, we discuss the design of fabrication-robust, high-FSR, and low-crosstalk mode-selective silicon MRRs for the TE_0, TE_1, TE_2, and TE_3 modes. By engineering the phase matching conditions between a single-mode ring resonator and multimode bus waveguides, the designed devices selectively couple a single higher-order spatial mode in a multimode bus waveguide to the fundamental TE_0 mode of a single-mode MRR, enabling mode-selective wavelength filtering while maintaining a compact 5 μm ring radius. Additionally, all selected modes are coupled out at the drop port as the fundamental TE_0 mode. To guide the device design, we derive analytical coupling constraints on the full width at half maximum (FWHM) and extinction ratio and combine these with systematic design space optimization to identify nominal device geometries that simultaneously satisfy the crosstalk, bandwidth, extinction ratio, and fabrication robustness requirements for practical deployment. The demonstrated mode-selective MRRs achieve FSRs up to 14.9 nm with nominal crosstalk suppression values of 30.3 dB, 39.1 dB, and 28.8 dB for the TE_1, TE_2, and TE_3 devices, respectively. Eye diagram and bit error rate (BER) measurements demonstrate 25 Gb/s transmission using NRZ PRBS31 signals with BERs below 10^{-12} for received optical powers of -7.5 dBm and above for all fabricated MRRs, with all eye diagrams remaining clearly open. Fabrication variation analysis further demonstrates robust performance under representative dimensional variations in waveguide geometry, with all designs maintaining crosstalk suppression between 23 dB and 40 dB between the desired mode and all lower-order modes. As summarized in Table 1, the demonstrated mode-selective MRRs simultaneously achieve high free spectral range (FSR), low crosstalk, compact footprint, and experimentally evaluated fabrication robustness, highlighting their potential as compact building blocks for high-speed integrated MDM photonic systems.

The paper is structured as follows: In Section 2, we present the analytical modeling, design space optimization, and simulation results of the mode-selective MRRs. Section 3 details the experimental characterization, high-speed transmission experiments, and fabrication tolerance analysis of the fabricated devices. Finally, Section 4 presents the conclusions.

2. Device design and simulation

2.1. Analytical design of mode-selective MRRs

We begin by considering the key performance requirements of the mode-selective microring resonators (MRRs). First, the MRRs must selectively couple the desired spatial mode while rejecting all other modes with high crosstalk suppression. We target a crosstalk suppression exceeding 20 dB, corresponding to less than 1% residual power coupled into undesired modes. Second, the MRRs must exhibit a sufficiently large Full Width at Half Maximum (FWHM) to support high-speed data transmission. Following the criterion that the resonance bandwidth should be at least twice the operating data rate, operation up to 25 Gbps requires a minimum FWHM of 50 GHz [26,27]. Third, the MRRs must provide a sufficiently high extinction ratio (ER) to clearly distinguish between the on and off states. We target an ER exceeding 20 dB to provide strong resonance contrast for filtering applications.

To achieve the first condition — a crosstalk suppression greater than 20 dB — we begin by determining the phase matching conditions between the MRR and the through port bus waveguides. Here, the crosstalk suppression is defined as the difference between the drop port transmission at the resonance wavelength when the targeted input mode is excited and the maximum drop port transmission when any other input mode is excited. Figure 1(a) illustrates the geometric parameters of the mode-selective MRRs. The MRR is designed with a compact radius of 5 μm in order to achieve a high FSR. A waveguide width of 0.400 μm is selected for the ring resonator to ensure single-mode operation in a 220 nm thick silicon waveguide. Each of the four targeted modes — TE_0, TE_1, TE_2, and TE_3 — requires a different bus waveguide width to satisfy the phase matching condition, where the effective index of the bus waveguide mode matches the effective index of the fundamental TE_0 mode of the MRR. Figure 1(b) shows the effective indices of the four modes as a function of the silicon waveguide width, calculated using Ansys Lumerical MODE. The dashed black line denotes the effective index of the single-mode ring resonator waveguide with a width of 0.400 μm, while the black circles denote the phase-matched widths for each mode. Matching the effective indices of the bus waveguide and ring resonator yields bus waveguide widths of approximately 0.405 μm for TE_0, 0.839 μm for TE_1, 1.265 μm for TE_2, and 1.694 μm for TE_3. These phase matching conditions provide the initial design parameters, which are subsequently refined through Ansys Lumerical FDTD optimization to account for the full electromagnetic coupling behavior of the mode-selective MRRs.

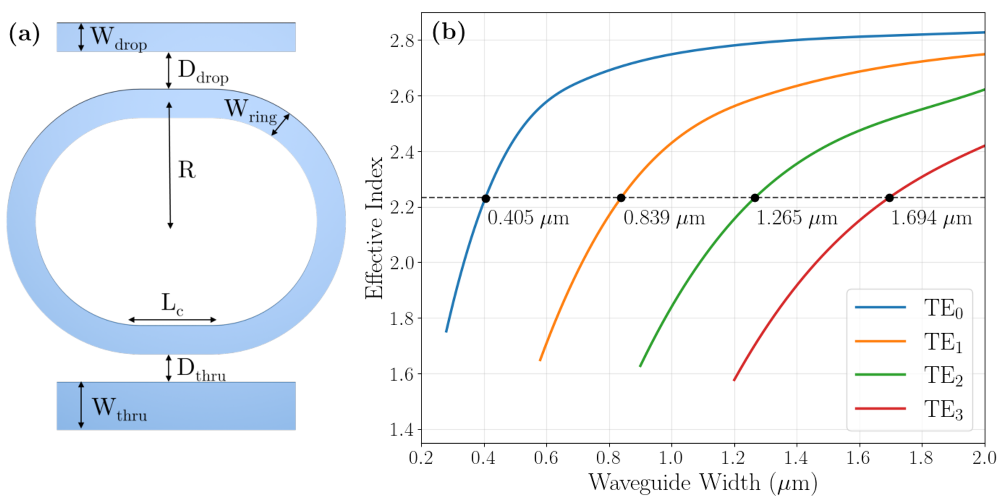

Fig. 1. **(a)**: Schematic of the geometric parameters of the mode-selective microring resonators. W_{thru}: through port waveguide width; W_{drop}: drop port waveguide width; W_{ring}: microring resonator waveguide width; D_{thru}: through port coupling gap; D_{drop}: drop port coupling gap; R: microring resonator radius; L_c: coupling length. **(b)**: Effective index as a function of waveguide width for the supported spatial modes. The dashed black line denotes the effective index of the single-mode microring resonator waveguide with a width of 0.400 μm. The black circles on each curve denote the phase matching conditions between the ring resonator and each supported mode in the multimode bus waveguide, where the effective indices of the two waveguides are matched to enable efficient optical coupling.

To satisfy the bandwidth requirement for high-speed operation, we next analyze the Full Width at Half Maximum (FWHM) of the mode-selective MRRs. For an add-drop ring resonator, the FWHM is given by

$$\mathrm{FWHM} = \frac{\lambda_{\mathrm{res}}^2 (1 - r_1 r_2 a)}{\pi n_g L \sqrt{r_1 r_2 a}}, \tag{1}$$

where λ_{res} is the resonance wavelength, n_g is the group index of the waveguide, L is the round-trip length of the resonator, r_1 and r_2 are the self-coupling coefficients of the couplers, and a is the round-trip field transmission factor, including both propagation loss in the ring and coupler loss [22]. The FWHM in Eq. (1) is converted to frequency units according to

$$\mathrm{FWHM}_f = \frac{c}{\lambda_{\mathrm{res}}^2}\mathrm{FWHM}_\lambda, \tag{2}$$

where c is the speed of light. For our design, we target a resonance wavelength of 1550.0 nm and operation near the critical coupling condition to achieve high extinction ratio while maintaining a sufficiently large bandwidth. The group index of the 0.400 μm silicon waveguide is calculated using Ansys Lumerical MODE, yielding $n_g = 4.45$, and the typical propagation loss of silicon is approximately 3.0 dB/cm [28]. Using these parameters, achieving a minimum FWHM of 50 GHz requires a minimum cross-coupling coefficient of $\kappa_1^2 = 0.080$, where $\kappa_1^2 + r_1^2 = 1$.

Finally, to ensure clear discrimination between the on- and off-resonance states, we analyze the extinction ratio (ER) of the mode-selective MRRs. For an add-drop ring resonator, the extinction ratio is defined as [22]

$$\mathrm{ER}_{\mathrm{dB}} = 10 \log_{10}\left(\frac{T_{\max}}{T_d}\right), \tag{3}$$

where

$$T_{\max} = \frac{\left(1 - r_1^2\right)\left(1 - r_2^2\right) a}{(1 - r_1 r_2 a)^2} \tag{4}$$

$$T_d = \frac{\left(1 - r_1^2\right)\left(1 - r_2^2\right) a}{(1 + r_1 r_2 a)^2} \tag{5}$$

Using Eqs. (4) and (5), we find that to achieve an ER greater than 20 dB, the cross-coupling coefficient must satisfy $\kappa_1^2<0.180$. Combining the conditions for the FWHM and ER yields the design constraint $0.080<\kappa_1^2<0.180$.

In the following section, we combine the phase matching requirements with the coupling coefficient design constraints to perform parameter sweeps and optimize the MRR geometry in order to satisfy the crosstalk suppression requirements.

2.2. Device optimization and simulation results

Starting from the phase-matched widths determined earlier, we perform parameter sweeps to optimize the coupling coefficient and maximize the crosstalk suppression for each of the mode-selective MRRs. The nominal through port widths are initialized using the phase-matched widths determined in Fig. 1(b), and Ansys Lumerical FDTD is used to optimize the coupling between the through port waveguide and the ring by sweeping the through port width W_{thru}, through port coupling gap D_{thru}, and coupling length L_{c}. Figure 2 summarizes representative design spaces obtained by sweeping D_{thru} and L_{c}, while the remaining device parameters are fixed at their final nominal values listed in Table 2. The corresponding through port power coupling coefficient, crosstalk suppression, extinction ratio, and FWHM are shown for each mode-selective MRR. In addition to identifying operating points that satisfy the crosstalk, extinction ratio, and bandwidth requirements, the design spaces enable selection of nominal device geometries located within relatively broad high-performance regions, thereby improving robustness to fabrication-induced

Optics EXPRESS

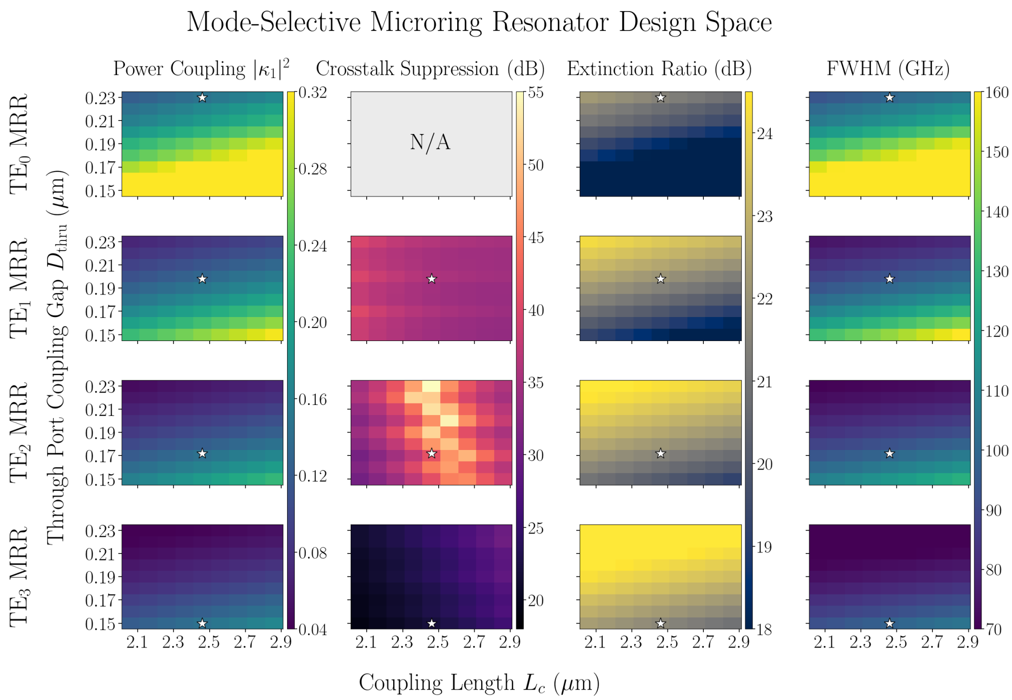

Fig. 2. Representative design spaces for the fabricated TE_0, TE_1, TE_2, and TE_3 mode-selective MRRs. The through port power coupling coefficient (κ_1^2), crosstalk suppression, extinction ratio (ER), and full width at half maximum (FWHM) are shown as functions of the through port coupling gap D_{thru} and coupling length L_{c}, while the remaining device parameters are fixed at their nominal values listed in Table 2. The selected nominal device geometries are indicated by the white star markers and correspond to operating points that simultaneously satisfy the crosstalk, extinction ratio, and bandwidth requirements while remaining within broad high-performance regions for improved fabrication robustness. Crosstalk suppression is not reported for the TE_0 MRR because no lower-order mode is present for this case.

dimensional variations. As shown in Fig. 2, increasing the coupling strength generally improves the crosstalk suppression and FWHM, but reduces the extinction ratio, resulting in a well-defined design region that satisfies all three performance metrics. The selected nominal designs, indicated by the star markers in Fig. 2, correspond to operating points that simultaneously satisfy the crosstalk suppression, extinction ratio, and bandwidth requirements while maintaining a common coupling length for all four mode-selective MRRs to maintain consistent resonance wavelengths and FSRs. The drop port waveguide geometry for each mode-selective MRR is designed using the same coupling geometry as the TE_0 through port configuration, enabling efficient coupling of the dropped signal into the fundamental TE_0 mode while maintaining operation near the critical coupling condition. The full MRR spectra are simulated using Ansys Lumerical FDTD and Ansys Lumerical INTERCONNECT. The simulated drop and through port spectra are shown in Fig. 3, and the final design parameters and simulated performance metrics are summarized in Table 2. The drop port spectra demonstrate selective coupling of the targeted spatial mode, while the through port spectra show that the targeted mode is removed from the through port and the lower-order non-target modes remain largely undisturbed. All four mode-selective MRRs exhibit crosstalk suppression values above 20 dB, FWHM greater than 50 GHz, and extinction ratios above 20 dB. Together, these results demonstrate that the mode-selective MRRs provide mode-

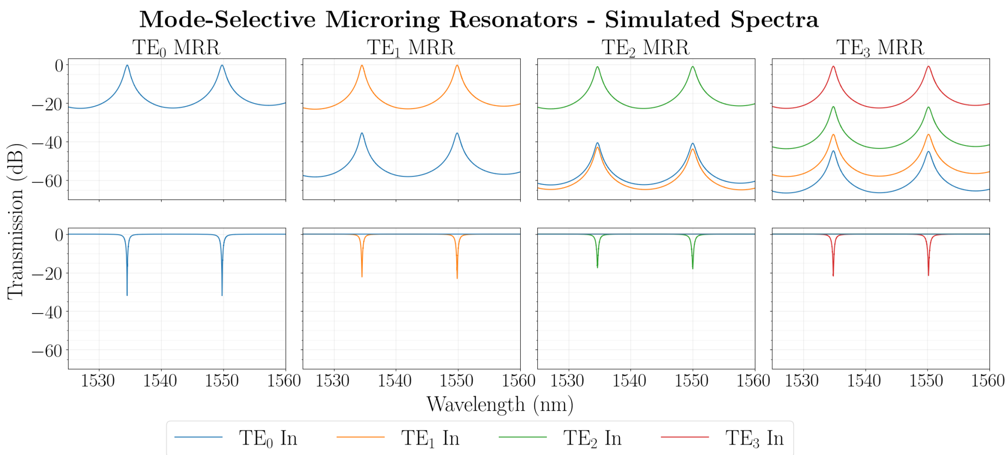

Fig. 3. Simulated drop port (top row) and through port (bottom row) transmission spectra of the TE_0, TE_1, TE_2, and TE_3 mode-selective MRRs. The drop port spectra demonstrate wavelength-selective coupling for the targeted spatial mode while suppressing coupling to the remaining modes. The through port spectra demonstrate negligible interaction between the mode-selective MRR and the non-target spatial modes, while the targeted spatial mode is selectively filtered by the ring. The simulated performance metrics are summarized in Table 2.

and wavelength-selective filtering with high modal isolation, sufficiently large bandwidth for high-speed operation, and strong resonance contrast. In the following section, we present the experimental characterization of the fabricated mode-selective MRRs.

Table 2. Optimized parameters and performance metrics of the simulated mode-selective microring resonators. W_{thru}: through port waveguide width; D_{thru}: through port coupling gap; W_{drop}: drop port waveguide width; D_{drop}: drop port coupling gap; κ_1^2: through port power cross-coupling coefficient; κ_2^2: drop port power cross-coupling coefficient; *a*: round-trip field transmission factor; *XT*: crosstalk suppression; *FWHM*: full width at half maximum; *Q*: loaded quality factor; *ER*: extinction ratio; *IL*: insertion loss.

Mode	W_{thru}	D_{thru}	W_{drop}	D_{drop}	κ_1^2	κ_2^2	a	XT (dB)	FWHM (GHz)	Q	ER (dB)	IL (dB)
TE_0	0.400	0.230	0.400	0.230	0.1465	0.1465	0.98951	–	102.5	1880.7	22.2	0.21
TE_1	0.832	0.198	0.400	0.230	0.1353	0.1465	0.99139	35.2	97.4	1975.5	22.6	0.23
TE_2	1.268	0.172	0.400	0.230	0.1399	0.1465	0.97687	39.8	108.0	1781.2	21.7	0.94
TE_3	1.708	0.150	0.400	0.230	0.1436	0.1465	0.97626	21.2	109.6	1753.9	21.6	0.80

3. Experimental characterization

3.1. Measured device performance

Using the optimized design parameters from the previous section, the mode-selective MRRs were fabricated through an Applied Nanotools Inc. silicon multi-project wafer (MPW) run. Scanning electron microscope (SEM) images of the fabricated nominal mode-selective MRRs are shown in Fig. 4(a), highlighting the variation in the through port waveguide widths and through port coupling gaps for the different targeted modes. Figure 4(b) shows the fabricated test structure used for experimental characterization, consisting of an adiabatic coupler (ADC)-based mode multiplexer and a single mode-selective MRR. In each test structure, the ADC mode multiplexer converts the fundamental TE_0 mode excited by the grating couplers into the higher-order spatial modes supported by the multimode through port bus waveguide. Figure 4(c) shows the cascaded ADC mode multiplexer and demultiplexer test structure used to experimentally characterize the ADC mode converters. The ADC mode multiplexer enables selective excitation of the TE_0, TE_1, TE_2, and TE_3 spatial modes in the central multimode waveguide. The corresponding ADC mode demultiplexer converts each supported spatial mode back to the fundamental TE_0 mode, enabling characterization of the modal crosstalk and conversion efficiency summarized in Table 3. The purpose of this characterization is to verify selective excitation of the intended spatial modes prior to characterization of the mode-selective MRRs. The mode converters exhibit crosstalk suppression greater than 23 dB across at least the wavelength range from 1516–1565 nm. Using the characterized ADC mode multiplexer, each supported spatial mode is individually excited in the through port of the mode-selective MRR. The selected mode is then coupled by the MRR to the drop port as the fundamental TE_0 mode, where the resulting transmission is measured. All transmission spectra reported in this work are measured using a broadband optical spectrum analyzer (BOSA) with a measurement noise floor of approximately −80 dB.

Table 3. Measured mode conversion performance of the cascaded adiabatic coupler (ADC)-based mode multiplexer and demultiplexer at 1550 nm. The optical power measured at each output port for excitation of the TE_0, TE_1, TE_2, and TE_3 input ports demonstrates selective mode conversion and low modal crosstalk.

Input Mode	TE_0 Output	TE_1 Output	TE_2 Output	TE_3 Output
TE_0	-1.1 dB	-38.0 dB	-42.8 dB	-42.3 dB
TE_1	-39.7 dB	-1.5 dB	-36.0 dB	-50.1 dB
TE_2	-42.0 dB	-33.5 dB	-1.1 dB	-30.3 dB
TE_3	-50.2 dB	-54.5 dB	-33.4 dB	-1.3 dB

To evaluate the robustness of the nominal designs, multiple geometrical variations of each mode-selective MRR were fabricated and experimentally characterized, including intentional variations in the through port waveguide width W_{thru}, through port coupling gap D_{thru}, drop port coupling gap D_{drop}, and coupling length L_c. Relative to the nominal design, W_{thru} and L_c are varied by ±40 nm, while D_{thru} and D_{drop} are varied by ±20 nm. The measured drop port spectra for fabricated TE_0, TE_1, TE_2, and TE_3 mode-selective MRRs are shown in Fig. 5. The corresponding through port transmission spectra for the targeted spatial mode are overlaid as dashed lines, confirming wavelength-selective filtering of the targeted spatial mode in the through port. The measured performance of the nominal device designs is summarized in Table 4. The corresponding coupling coefficients and round-trip field transmission factor are extracted from the measured resonance spectra using a joint nonlinear optimization. All nominal mode-selective MRRs exhibit crosstalk suppression greater than 28.8 dB, FWHM greater than 71.7 GHz, ER greater than 23.1 dB, and FSRs of approximately 14.9 nm. The reduced FWHM and increased drop port extinction ratio relative to simulation are consistent with the lower coupling coefficients extracted from the experimental spectra, as weaker coupling results in narrower resonance linewidths and higher drop port extinction ratios. The higher measured TE_3 crosstalk suppression relative to simulation is also consistent with the lower extracted coupling coefficient. As shown in Fig. 2, the TE_3 design space includes weaker-coupling operating regions with higher crosstalk suppression because the parasitic coupling of the TE_2 mode from the through port waveguide into the MRR decreases more rapidly than the desired TE_3 coupling in this regime.

3.2. Bit error rate and eye diagrams

We then perform high-speed data transmission experiments to characterize the signal integrity performance of the mode-selective MRRs. The experimental setup is shown in Fig. 6(a). A Thorlabs MX35E linear transmitter, which includes both a continuous-wave (CW) tunable

Optics EXPRESS

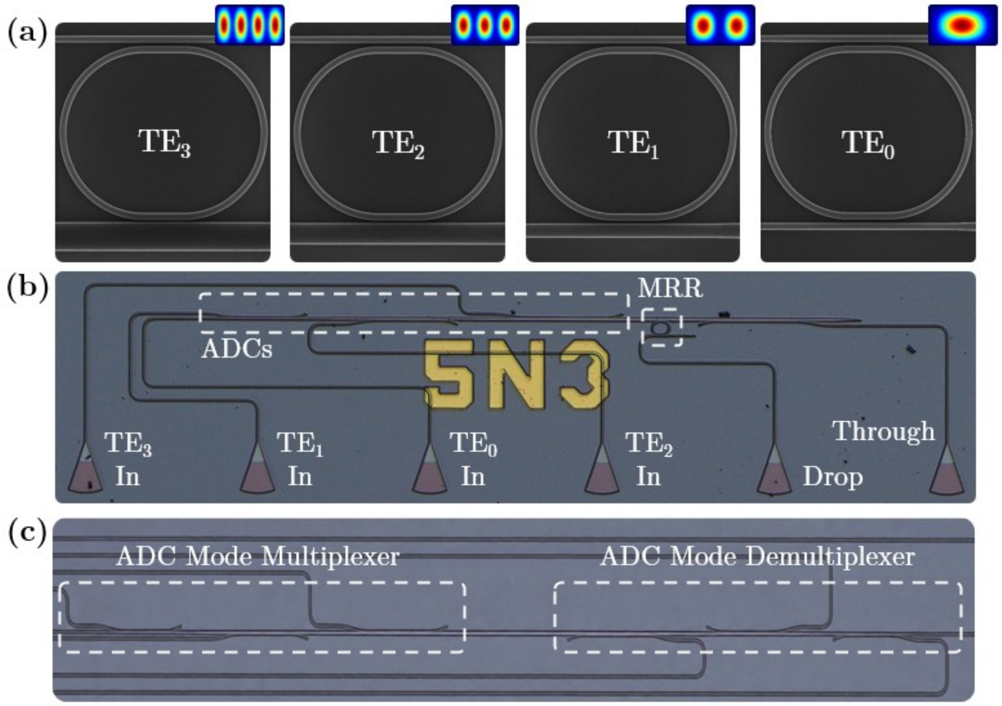

Fig. 4. **(a)** Scanning electron microscope (SEM) images of the fabricated mode-selective MRRs. **(b)** Optical microscope image of a fabricated test structure used for experimental characterization. The image shows a TE_3 mode-selective MRR test structure, consisting of an adiabatic coupler (ADC)-based mode multiplexer and a single mode-selective MRR. Light is coupled into the chip as the fundamental TE_0 mode through the grating couplers, and the ADC mode multiplexer selectively excites the TE_0, TE_1, TE_2, and TE_3 spatial modes in the multimode through port waveguide by choosing the corresponding input grating coupler. Equivalent test structures are fabricated for the TE_0, TE_1, and TE_2 mode-selective MRRs. The label "5N3" denotes a nominal TE_3 mode-selective MRR with a 5 μm radius. **(c)** Optical microscope image of the cascaded ADC mode multiplexer and demultiplexer test structure used to experimentally characterize the ADC mode converters. The ADC mode multiplexer enables selective excitation of the TE_0, TE_1, TE_2, and TE_3 spatial modes in the central multimode waveguide. The corresponding ADC mode demultiplexer converts each supported spatial mode back to the fundamental TE_0 mode, enabling characterization of the modal crosstalk and conversion efficiency summarized in Table 3.

laser source (TLS) and optical modulator, is used to generate the modulated optical signal at a wavelength of 1548.51 nm. Modulation is driven using an Anritsu MP1900A pulse pattern generator (PPG) with a non-return-to-zero (NRZ) pseudo-random bit sequence of length $2^{31} - 1$ (PRBS31). The optical signal is amplified using an erbium-doped fiber amplifier (EDFA) to compensate for grating coupler insertion loss and is coupled into the chip through a single-mode fiber (SMF) after passing through a polarization controller (PC). The transmitted optical signal is coupled back into SMF, amplified using a second erbium-doped fiber amplifier (EDFA), and detected using a 40 GHz bandwidth Thorlabs RXM40AF photodetector (PD). A Keysight N7764A variable optical attenuator (VOA) is placed before the photodetector input for bit error rate (BER) characterization. The detected electrical signal is monitored using a Keysight N1092C sampling oscilloscope for eye diagram analysis and is also routed back to the PPG for BER

Optics EXPRESS

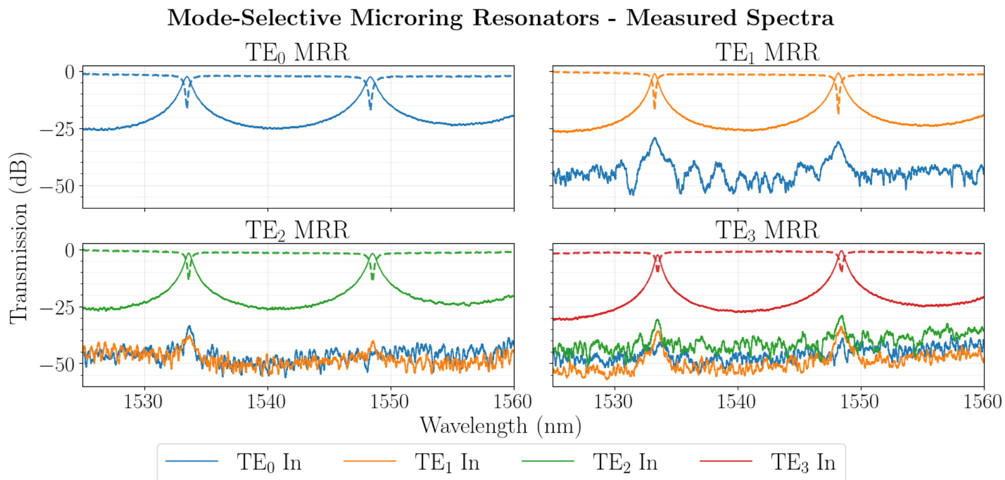

Fig. 5. Measured spectra of the fabricated TE_0, TE_1, TE_2, and TE_3 mode-selective MRRs. Solid curves show the drop port transmission spectra, while dashed curves show the corresponding through port transmission spectra for the targeted spatial mode. All devices exhibit strong mode- and wavelength-selective filtering with free spectral ranges (FSRs) of approximately 14.9 nm. The fabricated TE_1, TE_2, and TE_3 mode-selective MRRs demonstrate crosstalk suppression values of 30.3 dB, 39.1 dB, and 28.8 dB, respectively, while all devices maintain extinction ratios greater than 23.1 dB and FWHMs greater than 71.7 GHz, as summarized in Table 4.

Table 4. Measured performance and extracted fitting parameters of the nominal mode-selective MRRs. *XT*: crosstalk suppression; *FWHM*: full width at half maximum; *Q*: loaded quality factor; *ER*: extinction ratio; *IL*: insertion loss. The power cross-coupling coefficients (κ_1^2 and κ_2^2) and round-trip field transmission factor (*a*) are extracted from the measured through and drop port spectra using a joint nonlinear optimization.

Mode	XT (dB)	FWHM (GHz)	Q	ER (dB)	IL (dB)[a]	κ_1^2	κ_2^2	a
TE_0	–	84.6	2288.7	23.1	1.05	0.1232	0.1197	0.98978
TE_1	30.3	71.7	2700.7	25.0	0.86	0.1003	0.1163	0.99184
TE_2	39.1	79.1	2447.9	24.0	0.86	0.0951	0.1282	0.98750
TE_3	28.8	77.9	2485.4	23.3	0.60	0.0917	0.1361	0.99099

[a] Variations due to grating coupler performance and measurement alignment may contribute to the reported values.

testing. The oscilloscope receives a clock trigger directly from the PPG and pattern-locks to the transmitted PRBS31 signal.

The measured BER results are shown in Fig. 6(b). All mode-selective MRRs achieve BER below 10^{-12} at 25 Gbps for received optical powers of -7.5 dBm and above, where the received optical power is measured at the input of the photodetector. Each NRZ PRBS31 signal is transmitted continuously for approximately 2 minutes, corresponding to approximately 3×10^{12} transmitted bits and a 95% confidence level. The corresponding open eye diagrams are shown in Fig. 6(c). A loopback measurement consisting only of the input and output grating couplers is included for reference. The variation in BER sensitivity for each mode-selective MRR is likely influenced by path-dependent coupling differences, as well as slight laser detuning from the resonance wavelength. Because the transmitted power and resonance slope vary with wavelength detuning, small offsets from the resonance peak can increase the required received power. These

Optics EXPRESS

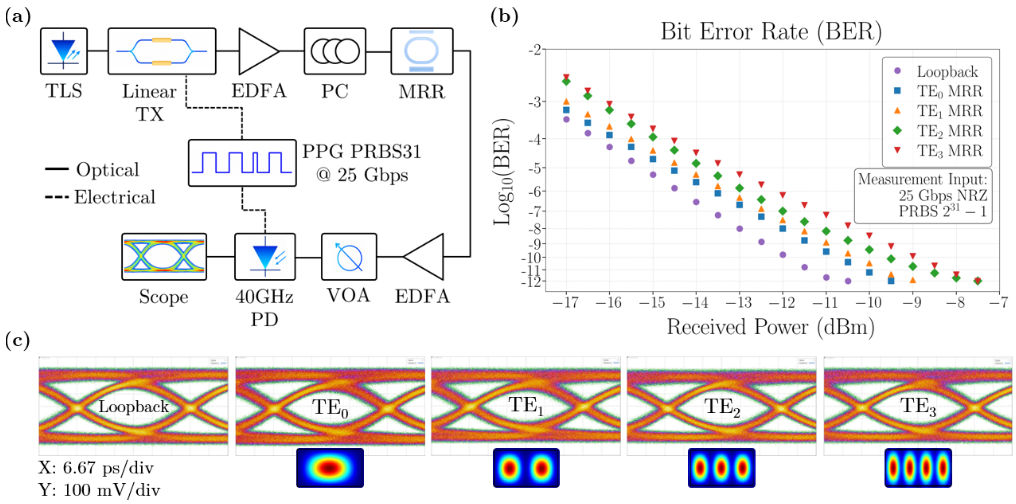

Fig. 6. **(a)** Experimental setup for the eye diagram and bit error rate (BER) characterization of the mode-selective MRRs. *TLS*: tunable laser source; *TX*: transmitter; *EDFA*: erbium-doped fiber amplifier; *PC*: polarization controller; *PPG*: pulse pattern generator; *PRBS31*: pseudo-random bit sequence of length $2^{31}-1$; *VOA*: variable optical attenuator; *PD*: photodiode; *NRZ*: non-return-to-zero. **(b)** Measured BER as a function of received optical power for the fabricated mode-selective MRRs at 25 Gbps. A loopback reference measurement consisting only of input and output grating couplers is included for comparison. All mode-selective MRRs demonstrate BERs below 10^{-12} for received optical powers of -7.5 dBm and above. **(c)** Measured open eye diagrams at 25 Gbps with NRZ PRBS31. All eye diagrams are shown using a horizontal scale of 6.67 ps/div and a vertical scale of 100 mV/div.

results demonstrate the ability of the mode-selective MRRs to support high-speed mode-selective filtering for integrated MDM photonic systems.

3.3. Fabrication tolerance analysis

Finally, we characterize the performance of the fabricated MRR variants to evaluate the fabrication tolerance of the mode-selective MRRs. Typical fabrication variations arising from lithography and etch process biases can result in approximately ±10 nm deviations in waveguide widths and coupling gaps [29–31]. To evaluate the robustness of the nominal mode-selective MRR designs, we fabricated devices with intentional variations in the through port waveguide width W_{thru}, through port coupling gap D_{thru}, drop port coupling gap D_{drop}, and coupling length L_c. Relative to the nominal design, W_{thru} and L_c are varied by ±40 nm, while D_{thru} and D_{drop} are varied by ±20 nm. Although variations in L_c do not directly correspond to fabrication-induced variations, they are included to evaluate the sensitivity of the devices to the coupling length. These results are highlighted in Fig. 7. Each panel shows the distribution of measured performance across the fabricated variants for each mode-selective MRR, with individual markers corresponding to the fabricated variants. The boxes span the interquartile range from the 25th to 75th percentile, with the horizontal line inside each box indicating the median and the whiskers indicating the spread of the remaining measured values. The dashed horizontal lines indicate the target performance thresholds. Across the fabricated variants, all measured devices maintain extinction ratios above 22 dB and FWHM values above 53 GHz, while the measured crosstalk suppression remains above 23 dB for the TE$_1$, TE$_2$, and TE$_3$ devices, showing that all fabricated variants continue to satisfy the original target metrics despite the introduced dimensional perturbations.

Optics EXPRESS

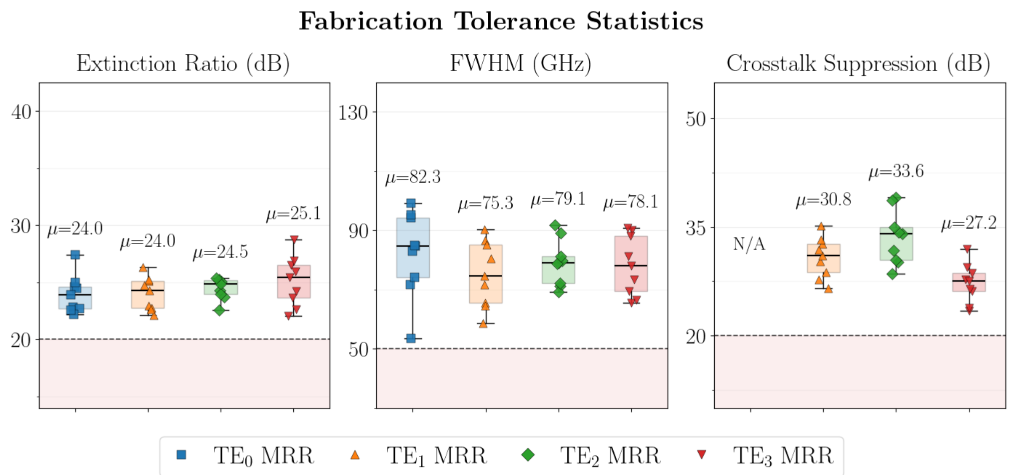

Fig. 7. Measured fabrication tolerance statistics of the fabricated mode-selective MRR variants. The distributions summarize the measured extinction ratio, FWHM, and crosstalk suppression across perturbations in the through port waveguide width W_{thru}, through port coupling gap D_{thru}, drop port coupling gap D_{drop}, and coupling length L_c. Markers show individual fabricated variants. Each box spans the interquartile range from the 25th to 75th percentile, with the horizontal line inside the box indicating the median; the whiskers indicate the spread of the remaining measured values; the annotated μ values indicate the mean measured value for each distribution; and dashed horizontal lines indicate the target performance thresholds. Crosstalk suppression is not shown for the TE_0 MRR because no lower-order mode is present for comparison. All measured variants maintain extinction ratios above 22 dB and FWHM values above 53 GHz, while the measured crosstalk suppression remains above 23 dB for the TE_1, TE_2, and TE_3 MRRs.

The mean extinction ratios are 24.0, 24.0, 24.5, and 25.1 dB for the TE_0, TE_1, TE_2, and TE_3 MRRs, respectively, indicating consistently high extinction across all four mode-selective designs. The FWHM distributions show mean values of 82.3, 75.3, 79.1, and 78.1 GHz, respectively, with the TE_0 device exhibiting the largest average linewidth. The crosstalk suppression is highest for the TE_2 MRR, with a mean value of 33.6 dB, followed by the TE_1 and TE_3 MRRs with mean crosstalk suppressions of 30.8 and 27.2 dB. The perturbed variants remain close to the nominal measured performance described in Table 4, indicating that the explored dimensional changes do not degrade the device performance. Differences in the distribution widths arise from variations in the fabricated coupling coefficients, as well as from mode-dependent sensitivity to the explored dimensional perturbations. Crosstalk suppression is not reported for the TE_0 device because no lower-order mode is present for this case. Although the fabrication robustness analysis does not explicitly isolate the effects of process-induced sidewall roughness and local dimensional nonuniformities, these effects are inherently present in the fabricated devices and intentional geometric variants characterized in this work. Overall, the measured distributions confirm that the mode-selective MRRs remain robust under realistic fabrication-induced dimensional variations.

4. Conclusion

In this work, we have demonstrated fabrication-robust, high-FSR, and low-crosstalk mode-selective microring resonators (MRRs) for integrated mode-division multiplexing (MDM) systems. By engineering the phase matching conditions between a single-mode ring resonator and multimode bus waveguides, we experimentally demonstrate mode- and wavelength-selective filtering for the TE_0, TE_1, TE_2, and TE_3 spatial modes. The fabricated devices exhibit crosstalk suppression greater than 28.8 dB, extinction ratios greater than 23.1 dB, FWHMs greater than 71.7 GHz, and FSRs of approximately 14.9 nm. Eye diagram and bit error rate (BER) experiments further demonstrate 25 Gb/s operation with BERs below 10^{-12} for received optical powers of −7.5 dBm and above for all fabricated mode-selective MRRs, with all eye diagrams remaining open. Additionally, all dropped signals are coupled out as the fundamental TE_0 mode, simplifying integration with downstream single-mode photonic components. Fabrication variation analysis further demonstrates robust operation under expected process-induced dimensional variations. These results establish mode-selective MRRs as a promising building block for compact, high-speed, and scalable integrated MDM photonic systems. Future work will focus on integrating the mode-selective MRRs into larger mode- and wavelength-selective photonic systems, incorporating established thermal tuning and resonance-locking techniques to enable stable operation under practical operating conditions, and investigating the impact of stochastic fabrication variations, including nonuniform dimensional fluctuations and sidewall roughness, on device performance [32,33].

Funding. Center for Ubiquitous Connectivity (CUbiC).

Acknowledgment. The chip fabrication and scanning electron microscope (SEM) imaging were performed by Applied Nanotools Inc. in Edmonton, Alberta, Canada through a silicon multi-project wafer (MPW) service. This work was supported in part by the Center for Ubiquitous Connectivity (CUbiC), one of the seven centers sponsored by the Semiconductor Research Corporation (SRC) and DARPA under the Joint University Microelectronics Program 2.0 (JUMP 2.0).

Disclosures. The authors declare no conflicts of interest.

Data availability. Data underlying the results presented in this paper are not publicly available at this time but may be obtained from the authors upon reasonable request.

References

1. D. Narayanan, M. Shoeybi, J. Casper, *et al.*, "Efficient large-scale language model training on gpu clusters using megatron-lm," in *Proceedings of the international conference for high performance computing, networking, storage and analysis*, (2021), pp. 1–15.
2. Q. Cheng, M. Bahadori, M. Glick, *et al.*, "Recent advances in optical technologies for data centers: a review," Optica **5**(11), 1354–1370 (2018).
3. D. A. Miller, "Rationale and challenges for optical interconnects to electronic chips," Proc. IEEE **88**(6), 728–749 (2002).
4. S. Rumley, D. Nikolova, R. Hendry, *et al.*, "Silicon photonics for exascale systems," J. Lightwave Technol. **33**(3), 547–562 (2015).
5. R. Parsons, X. Meng, J. Robinson, *et al.*, "Silicon photonic integration of dwdm and mode-division multiplexing for advancing multi-dimensional data transmission," in *CLEO: Science and Innovations*, (Optica Publishing Group, 2024), pp. SF1O–5.
6. O. A. J. Gordillo, A. Novick, O. L. Wang, *et al.*, "Fiber-chip link via mode division multiplexing," IEEE Photonics Technol. Lett. **35**(19), 1071–1074 (2023).
7. L.-W. Luo, N. Ophir, C. P. Chen, *et al.*, "Wdm-compatible mode-division multiplexing on a silicon chip," Nat. Commun. **5**(1), 3069 (2014).
8. K. R. Mojaver, S. M. R. Safaee, S. S. Morrison, *et al.*, "Recent advancements in mode division multiplexing for communication and computation in silicon photonics," J. Lightwave Technol. **42**(22), 7860–7870 (2024).
9. H. Xu, D. Dai, and Y. Shi, "Silicon integrated nanophotonic devices for on-chip multi-mode interconnects," Appl. Sci. **10**(18), 6365 (2020).
10. R. Yin, H. Xiao, Y. Jiang, *et al.*, "Integrated wdm-compatible optical mode division multiplexing neural network accelerator," Optica **10**(12), 1709–1718 (2023).
11. K. Y. Yang, C. Shirpurkar, A. D. White, *et al.*, "Multi-dimensional data transmission using inverse-designed silicon photonics and microcombs," Nat. Commun. **13**(1), 7862 (2022).
12. Y. Su, Y. He, H. Chen, *et al.*, "Perspective on mode-division multiplexing," Appl. Phys. Lett. **118**(20), 200502 (2021).
13. H. Jia, X. Fu, T. Zhou, *et al.*, "Mode-selective modulation by silicon microring resonators and mode multiplexers for on-chip optical interconnect," Opt. Express **27**(3), 2915–2925 (2019).
14. A. Khaled, A. Aadhi, C. Huang, *et al.*, "Fully integrated hybrid multimode-multiwavelength photonic processor with picosecond latency," Nat. Commun. **17**(1), 28 (2025).
15. B. Stern, X. Zhu, C. P. Chen, *et al.*, "On-chip mode-division multiplexing switch," Optica **2**(6), 530–535 (2015).

16. S. M. R. Safaee, K. R. Mojaver, G. Zhang, *et al.*, "Silicon photonics mode-selective phase shifter," J. Lightwave Technol. **42**(7), 2412–2421 (2023).
17. H. Jia, S. Yang, T. Zhou, *et al.*, "Wdm-compatible multimode optical switching system-on-chip," Nanophotonics **8**(5), 889–898 (2019).
18. Y. Zhao, X. Ji, B. Y. Kim, *et al.*, "Visible nonlinear photonics via high-order-mode dispersion engineering," Optica **7**(2), 135–141 (2020).
19. A. Shamsshooli, Y. Kwon, C. Guo, *et al.*, "Devices for quantum communication over mode-division-multiplexing systems," in *Quantum Computing, Communication, and Simulation III*, vol. 12446 (SPIE, 2023), pp. 78–81.
20. S. Koudia, L. Oleynik, J. Ur Rehman, *et al.*, "Spatial-mode diversity and multiplexing for continuous variables quantum communications," Commun. Phys. **8**(1), 351 (2025).
21. C. Li, D. Liu, and D. Dai, "Multimode silicon photonics," Nanophotonics **8**(2), 227–247 (2019).
22. W. Bogaerts, P. De Heyn, T. Van Vaerenbergh, *et al.*, "Silicon microring resonators," Laser photonics reviews **6**(1), 47–73 (2012).
23. X. Han, H. Xiao, Z. Liu, *et al.*, "Reconfigurable on-chip mode exchange for mode-division multiplexing optical networks," J. Lightwave Technol. **37**(3), 1008–1013 (2018).
24. H. Jia, X. Fu, T. Zhou, *et al.*, "Interface of electrical data-bus to multimode optical data-bus using racetrack microring resonators," IEEE Photonics Technol. Lett. **31**(17), 1397–1400 (2019).
25. Y.-D. Yang, Y. Li, Y.-Z. Huang, *et al.*, "Silicon nitride three-mode division multiplexing and wavelength-division multiplexing using asymmetrical directional couplers and microring resonators," Opt. Express **22**(18), 22172–22183 (2014).
26. A. Novick, A. James, L. Dai, *et al.*, "High-bandwidth density silicon photonic resonators for energy-efficient optical interconnects," Appl. Phys. Rev. **10**(4), 041306 (2023).
27. S. Daudlin, A. Rizzo, S. Lee, *et al.*, "Three-dimensional photonic integration for ultra-low-energy, high-bandwidth interchip data links," Nat. Photonics **19**(5), 502–509 (2025).
28. Q. Liu, Y. Bian, and J. Xiong, "Progress in passive silicon photonic devices: A review," in *Photonics*, vol. 12 (MDPI, 2025), p. 928.
29. Y. Xing, J. Dong, U. Khan, *et al.*, "Capturing the effects of spatial process variations in silicon photonic circuits," ACS Photonics **10**, 928–944 (2023).
30. M. Nikdast, G. Nicolescu, J. Trajkovic, *et al.*, "Chip-scale silicon photonic interconnects: A formal study on fabrication non-uniformity," J. Lightwave Technol. **34**(16), 3682–3695 (2016).
31. Y. Wang, A. Novick, R. Parsons, *et al.*, "Scalable architecture for sub-pJ/b multi-Tbps comb-driven DWDM silicon photonic transceiver," in *Next-Generation Optical Communication: Components, Sub-Systems, and Systems XII*, vol. 12429 G. Li, K. Nakajima, and A. K. Srivastava, eds., International Society for Optics and Photonics (SPIE, 2023), p. 124291F.
32. K. Padmaraju and K. Bergman, "Resolving the thermal challenges for silicon microring resonator devices," Nanophotonics **3**(4-5), 269–281 (2014).
33. A. James, A. Rizzo, Y. Wang, *et al.*, "Process variation-aware compact model of strip waveguides for photonic circuit simulation," J. Lightwave Technol. **41**, 2801–2814 (2023).